http://www.diva-portal.org

Permanent link to this version:
http://urn.kb.se/resolve?urn=urn:nbn:se:kth:diva-307207

Evaluation of Hoffman and Xia plasticity models against bi-axial tension experiments of planar fiber network materials

Mossab Alzweighi [a,*], Rami Mansour [a], Johan Tryding [b,c], Artem Kulachenko [a]

[a] *Solid Mechanics, Department of Engineering Mechanics, KTH Royal Institute of Technology, SE-100 44, Stockholm, Sweden*
[b] *Division of Solid Mechanics, Lund University, Ole Römers väg 1, 223 63 Lund, Sweden*
[c] *Tetra Pak, Ruben Rausings gata 2, 223 55 Lund, Sweden*

ARTICLE INFO

ABSTRACT

The anisotropic properties and pressure sensitivity are intrinsic features of the constitutive response of fiber network materials. Although advanced models have been developed to simulate the complex response of fibrous materials, the lack of comparative studies may lead to a dubiety regarding the selection of a suitable method. In this study, the pressure-sensitive Hoffman yield criterion and the Xia model are implemented for the plane stress case to simulate the mechanical response under a bi-axial loading state. The performance of both models is experimentally assessed by comparison to bi-axial tests on cruciform-shaped specimens loaded in different directions with respect to the material principal directions. The comparison with the experimentally measured forces shows the ability of the Hoffman model as well as the Xia model with shape parameter $k \leq 2$ to adequately predict the material response. However, this study demonstrates that the Xia model consistently presents a stiffer bi-axial response when $k \geq 3$ compared to the Hoffman model. This result highlights the importance of calibrating the shape parameter k for the Xia model using a bi-axial test, which can be a cumbersome task. Also, for the same tension-compression response, the Hill criterion as a special case of the Hoffman model presents a good ability to simulate the mechanical response of the material for bi-axial conditions. Furthermore, in terms of stability criteria, the Xia model is unconditionally convex while the convexity of the Hoffman model is a function of the orthotropic plastic matrix. This study not only assesses the prediction capabilities of the two models, but also gives an insight into the selection of an appropriate constitutive model for material characterization and simulation of fibrous materials. The UMAT implementations of both models which are not available in commercial software and the calibration tool of the Xia model are shared with open-source along with this work.

1. Introduction

Bio-based materials are broadly used in modern industry due to their competitive bending stiffness vs. price, sustainability, lightness, and relatively good mechanical properties (Jungstedt et al., 2020; Wang et al., 2021). Also, the growing e-commerce trade results in a wider usage of bio-materials in different packaging applications where paper and paperboard have the largest volume in terms of production and usage (Srinivasa and Kulachenko, 2015).

The base structure of the paper material is the Fiber Network (FN). The small fibers bonded to each other due to hydrogen bonds (Roberts, 1996; Verma et al., 2014) are the main constitutive components of the FN. This FN presents heterogeneity (Hagman and Nygårds, 2017; Hristopulos and Uesaka, 2004), structural disorderliness (Alzweighi et al., 2021; Lahti et al., 2020), and anisotropy (Considine et al.,

2014) which result in difficulties in accurately predicting its mechanical performance.

The natural way of addressing the fiber network is the micromechanical approach which can include fiber properties, bonding between the fibers in the FN, and fibers alignment in 2D (Åström and Niskanen, 1993; Hägglund and Isaksson, 2008; Isaksson and Hägglund, 2007; Rigdahl et al., 1984) and 3D (Brandberg and Kulachenko, 2020; Heyden, 2000; Kulachenko and Uesaka, 2012). However, the complexity of the micro-mechanical models, difficulties in characterizing the properties of the fibers at the micro-level, and the prohibitive computational cost, limit the usage of direct FN simulations. Overcoming these limitations is crucial for the proper product scale design and reliability assessment (Hu et al., 2021) of fibrous materials.

For product development, it is a competitive advantage to introduce a modeling tool able to capture the investigated behavior of the material and suitable for practical applications. The continuum modeling approach is broadly employed to predict the mechanical response, as it is simpler to calibrate and is computationally efficient, see Seidlhofer et al. (2021), Mäkelä and Östlund (2003), Stenberg (2003), Beex and Peerlings (2009), Nygårds et al. (2009), Robertsson et al. (2018). In this approach, the material is often assumed to be homogeneous by neglecting the local variations. The material heterogeneity can however be accounted for by using stochastic spatial fields of model parameters, Monte-Carlo simulations and the stochastic finite-element (FE) method, see e.g. Mansour et al. (2019).

Different continuum models have been developed to replicate the anisotropic properties of bio-based materials. The most common anisotropic criterion used in paper modeling is the Hill criterion (Hill, 1948), which was employed to study the press forming process of paperboard (Awais et al., 2017) and to investigate creasing and folding (Huang et al., 2014). The Hill criterion has later been extended by Hoffman (1967) to account for different tension-compression properties (Bilko and Małyszko, 2020).

Another widely used method was proposed by Xia et al. (2002), in which the yield surface consists of 6 sub-surfaces to account for in-plane anisotropic plasticity as well as asymmetric tension-compression properties. Using Xia's potential, Nygårds (2009) modeled the in-plane elastic–plastic behavior of a multiply paperboard, and Tjahjanto et al. (2015) studied the viscoelastic-viscoplastic mechanical behavior of high dense cellulose-based materials. Li et al. (2016) proposed a modification of the Xia model, with a reduced number of the material parameters for a planar deformation incorporating nonlinear kinematic and isotropic hardening. Later, this criterion was extended to account for the out-of-plane plastic response (Borgqvist et al., 2015) and used for packaging forming study (Robertsson et al., 2018). A coupling between the sub-yield surfaces of the Xia model and a distortional hardening rule able to account for the sequence loading in different directions was also proposed by Borgqvist et al. (2014).

In the manufacturing process of paper and paperboard, a water solution containing fibers is sprayed onto a moving fabric web. As the fabric moves, the water-fibers solution drains through the fabric and the fibers orient and stack to form a paper which thereafter is dried. The process gives the paperboard its mechanical anisotropic properties and the material directions are named: Machine Direction (MD), the Cross-Machine direction (CD), and the thickness direction (ZD). It is noted that the process of stacking the fibers on each other gives mechanical properties in the MD-CD plane that is up to 100 times higher than the mechanical properties in ZD. Hence, it is assumed that the mechanical properties in the in-plane and out-of-plane (thickness direction) are uncoupled. This gives a zero Poisson's ratio in MD–ZD and CD–ZD. Here, also in-plane stress condition is assumed, i.e., the out-of-plane stresses are zero. Hence, due to the assumptions of mechanical uncoupling and plane stress, the out-of-plane strains are also zero.

In this work, the bi-axial loading condition on bio-based materials are investigated using three continuum models. Two models are based on the Hoffman yield criterion and one model is based on Xia's potential. The earlier studies for these models were mainly used for uni-axial loading and were not systematically compared against each other for the bi-axial loading case. The motivation for choosing those models stems from the intrinsic difference between them. The Hoffman model is of von Mises type while the Xia yield surface is composed of multi-surfaces. These types cover to a large extent most of the continuum model approaches for bio-based materials. Both models can present asymmetric tension-compression response which is an important feature in many materials including bio-based materials. However, the models are different in terms of material parameters and calibration strategy which are discussed in this work. The performance of both models is experimentally assessed by comparing the simulated mechanical response to bi-axial tests on cruciform-shaped specimens. The specimens are loaded in different directions with respect to the material principal directions. Furthermore, the Hoffman and Xia models are implemented into a user material routine (UMAT) using the general-purpose FE software Ansys. Both models are shared along with the publication to facilitate the simulation of anisotropic materials with different responses in tension-compression for academic and industrial applications.

This paper is organized as follows. In Section 2, the theory of the material models is presented. Section 3 presents the experimental setup used in the verification. In Section 4, the FE simulation is presented. Section 5 is devoted to the calibration of the models. Comparison between experiment and simulation is presented in Section 6.

2. Material model

In this Section, the Hoffman criterion and the Xia model are presented for the plane stress assumption, which is typical for paper and packaging applications. In Appendix the elastic–plastic equations and numerics outlying the models are presented, as they are referred to in the supplied source codes. The Hill model is also presented as a particular case of the Hoffman model.

2.1. Hoffman yield criterion

The Hoffman criterion is considered to be an extension of the Hill criterion with the ability to capture not only the anisotropic behavior but also the difference in tension-compression response. The Hoffman yield criterion can be written as (Hoffman, 1967),

$$f = \sigma_{eqv}^2 - \sigma_y^2(\kappa). \tag{1}$$

where σ_{eqv}, σ_y, and κ are the equivalent stress, hardening function, and internal hardening parameter, respectively. The equivalent stress is given by the sum of a quadratic and a linear term of the stress vector $\boldsymbol{\sigma}$ as

$$\sigma_{eqv} = \sqrt{\frac{1}{2}\boldsymbol{\sigma}^T \boldsymbol{P} \boldsymbol{\sigma} + \boldsymbol{q}^T \boldsymbol{\sigma}}. \tag{2}$$

where the stress vector for the in-plane case is defined as $\boldsymbol{\sigma} = [\sigma_{xx}, \sigma_{yy}, \sigma_{xy}]^T$. The subscripts xx and yy refer to the in-plane directions, MD and CD, whereas the subscript xy refers to the in-plane shear direction. The orthotropic plastic matrix, $\boldsymbol{P}$, in (2) describes the anisotropy of the material. Choosing the y-axis as the reference direction, i.e. $R_{yy} = 1$, and setting $R_{zz} = 1$, the $\boldsymbol{P}$ matrix can be written as

$$\boldsymbol{P} = 2 \begin{bmatrix} \frac{1}{R_{xx}^2} & \frac{-1}{2R_{xx}^2} & 0 \\ \frac{-1}{2R_{xx}^2} & 1 & 0 \\ 0 & 0 & \frac{3}{R_{xy}^2} \end{bmatrix}, \tag{3}$$

where R_{xx}, R_{yy}, R_{xy}, and R_{zz} are the ratio of the yield stresses in the xx, yy, xy, and zz directions, respectively, with respect to the reference yield stress and can be determined experimentally. The vector $\boldsymbol{q}$ features differences in yield stresses in tension and compression according to

$$\boldsymbol{q} = \begin{bmatrix} -\frac{\sigma_{xx}^{y,t} - \sigma_{xx}^{y,c}}{R_{xx}^2} \\ -\frac{\sigma_{yy}^{y,t} - \sigma_{yy}^{y,c}}{R_{yy}^2} \\ 0 \end{bmatrix}, \tag{4}$$

where the superscripts t and c stand for tension, and compression, respectively. From (2) for the case $\boldsymbol{q} = \boldsymbol{0}$, the Hill yield criterion is recovered. The main difference between the Hill and the Hoffman criteria, which both include the quadratic term of stresses, $\boldsymbol{\sigma}^T \boldsymbol{P} \boldsymbol{\sigma}$, is the linear term of stresses, i.e. $\boldsymbol{q}^T \boldsymbol{\sigma}$. This linear term implies that the sign of the stresses will affect the equivalent stress (pressure sensitivity).

The hardening function in (1) for isotropic hardening rule is given by

$$\sigma_y(\kappa) = \sigma_0 + K(\kappa), \qquad \text{where} \qquad K(\kappa) = H_0 \, \kappa^{1/n}. \tag{5}$$

In (5), σ_0, H_0, and n are the initial yield stress, hardening modulus, and hardening exponent, respectively. The internal hardening parameter, κ, is equal to the equivalent plastic strain, ε_{eqv}^p, i.e. $\kappa = \varepsilon_{eqv}^p$. The equivalent plastic strain is calculated from the plastic strain rate $\dot{\boldsymbol{\varepsilon}}^p$ according to

$$\dot{\varepsilon}_{eqv}^p = \sqrt{\frac{2}{3}(\dot{\boldsymbol{\varepsilon}}^p)^T \dot{\boldsymbol{\varepsilon}}^p}, \tag{6}$$

where the plastic strain rate vector is defined as $\dot{\boldsymbol{\varepsilon}}^p = [\dot{\varepsilon}_{xx}^p, \dot{\varepsilon}_{yy}^p, \dot{\varepsilon}_{xy}^p]^T$. The evolution of the plastic strains for associative plasticity is defined as $\dot{\boldsymbol{\varepsilon}}^p = \dot{\lambda}\frac{\partial f}{\partial \boldsymbol{\sigma}}$ (Dunne and Petrinic, 2005), where $\dot{\lambda}$ is the rate of the plastic multiplier.

2.2. Xia yield criterion

To model the anisotropic properties with a different tension-compression of paper material, Xia et al. (2002) introduced a non-quadratic yield surface that differs from the anisotropic yield criterion derived based on von Mises. The Xia potential for small strain and plane stress case can be presented as

$$f(\boldsymbol{\sigma}, K_\gamma) = \sum_{\gamma=1}^{6} \chi_\gamma \left(\frac{\boldsymbol{\sigma}^T \boldsymbol{N}_\gamma}{K_\gamma}\right)^{2k} - 1, \tag{7}$$

where γ is the number of sub-surfaces. The values $\gamma = 1$, 2, 3 represent tension in MD, tension in CD, and positive shear, respectively. The values $\gamma = 4$, 5, 6 are the sub-surfaces of compression in MD, compression in CD, and negative shear, respectively. A switch control χ_γ is defined as

$$\chi_\gamma = \begin{cases} 1 & \boldsymbol{\sigma}^T \boldsymbol{N}_\gamma > 0 \\ 0 & \text{otherwise.} \end{cases} \tag{8}$$

In (7), the exponent $2k$ is an even integer which controls the shape of the yield surface, K_γ is the hardening function of the sub-surfaces and $\boldsymbol{N}_\gamma$ are tensors describing the gradient of the sub-yield surfaces γ and are assumed to be of unit length as

$$\boldsymbol{N}_\gamma^T \boldsymbol{N}_\gamma = 1, \quad \boldsymbol{N}_\gamma = \sum_{i,j} n_{ij,\gamma} e_i e_j, \quad i, j = 1, 2. \tag{9}$$

Isotropic hardening for the Xia yield surface was introduced by Xia et al. (2002) for paperboard. However, uni-axial experimental tests in CD showed that the influence of pre-straining in MD up to failure is small (Borgqvist et al., 2014). When the uni-axial test was instead performed in MD, the pre-straining in CD had a higher influence on the strength to failure which decreased by approximately 17% (Borgqvist et al., 2014). Borgqvist et al. (2015) introduced uncoupled hardening to capture the paperboard with weak difference between a pre-strained or not pre-strained samples. Here, we adopt a similar uncoupled hardening with power hardening law K_γ defined as

$$K_\gamma(\kappa_\gamma) = K_{0,\gamma} + c_{1,\gamma}\kappa_\gamma^{1/c_{2,\gamma}}, \tag{10}$$

where $K_{0,\gamma}$ are hardening parameters, $c_{1,\gamma}$ and $c_{2,\gamma}$ are the hardening modulus and the hardening exponent, respectively. The evolution law for κ_γ is defined as,

$$\dot{\kappa}_\gamma = -\dot{\lambda}\frac{\partial f}{\partial K_\gamma}. \tag{11}$$

2.3. Comparison of the flow rule stability

Drucker (1963) presented a set of stability criteria for the non-linear stress–strain relation where the material is usually considered to be stable, in the sense of constitutive response, if it satisfies these postulates. Based on Drucker's stability postulates of elasto-plastic behavior,

the convexity of the yield function and the normality for associative plasticity are correlated with the material stability, cf. Justusson and Phillips (1966), Rudnicki and Rice (1975), Rice (1976). The normality of the plastic strain increment is satisfied for both Hoffman and Xia models as the plastic strain rate is parallel to the gradient of the loading function with respect to the stress.

The convexity shows that, for all possible $\boldsymbol{\sigma}^*$, the stress state $\boldsymbol{\sigma}^*$ should lie behind the borderline perpendicular to the plastic strain increment and this borderline must be a tangent to the yield surface. The convexity provides the uniqueness of the solution for the current stress tensor $\boldsymbol{\sigma}$. Furthermore, the yield function is convex in stress $\boldsymbol{\sigma}$, if its Hessian is positive semi-definite. For the Xia model, the Hessian is given by, cf. e.g. Ottosen and Ristinmaa (2005),

$$\boldsymbol{H}_{Xia} = \frac{\partial^2 f}{\partial \boldsymbol{\sigma}^2} = \sum_{\gamma=1}^{6} \chi_\gamma 2k(2k-1)\left(\frac{\boldsymbol{\sigma}^T \boldsymbol{N}_\gamma}{K_\gamma}\right)^{2k-2} \frac{\boldsymbol{N}_\gamma \boldsymbol{N}_\gamma^T}{K_\gamma^2} \geq 0. \tag{12}$$

Eq. (12) implies that the Xia yield function is unconditionally convex as this equation is always fulfilled. Similarly, for the Hoffman yield function, its Hessian can be written as

$$\boldsymbol{H}_{Hof} = \frac{\partial^2 f}{\partial \boldsymbol{\sigma}^2} = \boldsymbol{P} = \begin{bmatrix} P_{11} & P_{12} & 0 \\ & P_{22} & 0 \\ \text{Sym} & & P_{33} \end{bmatrix}. \tag{13}$$

From (13), the Hoffman yield surface is convex if the $\boldsymbol{P}$ matrix is positive semi-definite, i.e. if all its eigenvalues fulfill $\lambda_i \geq 0$, cf. e.g. Holzapfel (2002). These eigenvalues are given by

$$\begin{aligned} \lambda_1 &= P_{33} \geq 0 \\ \lambda_2 &= \frac{1}{2}\left(P_{11} + P_{22} + \sqrt{(P_{11}-P_{22})^2 + 4P_{12}^2}\right) \geq 0 \\ \lambda_3 &= \frac{1}{2}\left(P_{11} + P_{22} - \sqrt{(P_{11}-P_{22})^2 + 4P_{12}^2}\right) \geq 0. \end{aligned} \tag{14}$$

From (14), the eigenvalues λ_1 and λ_2 always satisfy the condition $\lambda_i \geq 0$. Meanwhile, for the third eigenvalue to be positive, the components of the orthotropic plastic matrix $\boldsymbol{P}$ shall fulfill the condition

$$P_{11} + P_{22} \geq \sqrt{(P_{11}-P_{22})^2 + 4P_{12}^2}. \tag{15}$$

The Hoffman yield surface is therefore convex if Eq. (15) is fulfilled, i.e. the model is conditionally convex.

3. Experimental setup

In this study, the cruciform shape is used for the bi-axial test. This shape is motivated by the ability to allow in-plane deformation of the material under different loading modes (Abu-Farha et al., 2009; Hannon and Tiernan, 2008; Smits et al., 2006). This shape was a subject of geometry optimization (Baptista et al., 2015), and investigation of its geometry influence on the estimation of the planar bi-axial mechanical properties (Hu et al., 2014). The cruciform shape was also used in other studies. For example, in Kiriyama et al. (2019) the authors developed bi-axial testing machine to get macroscopic information on elastoplastic deformation of thin specimens. Li et al. (2017) used it for a biaxial tensile-bending-combined micro-mechanical performance test. Zhao et al. (2019) introduced a sandwich cruciform specimen to obtain large plastic strains in the central zone of the specimen under bi-axial loading conditions.

The geometry of the specimen and its dimensions are presented in Fig. 1(a). These dimensions are chosen to be large enough to minimize the variation in the mechanical response of the material. The test was conducted using the bi-axial testing machine Zwick DO7144425 with two setups. In the first setup, the MD and CD directions coincide with the loading directions, as shown in Fig. 1(b) and the test is named the MD-CD Test. In the second setup, the MD and CD are rotated 45° with respect to the loading directions and named 45-Rot Test, as shown in Fig. 1(c). The displacements U_1, U_3, and U_2, U_4 applied by the axes
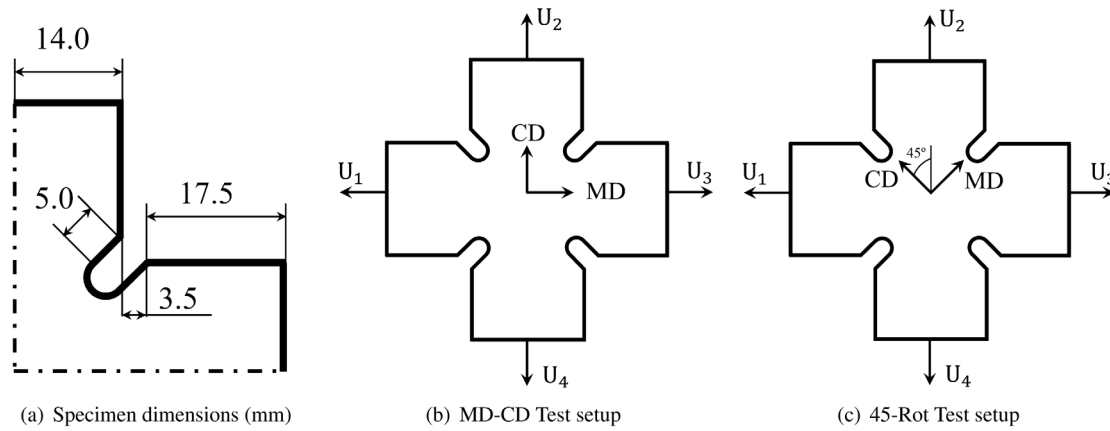
(a) Specimen dimensions (mm)   (b) MD-CD Test setup   (c) 45-Rot Test setup

Fig. 1. The cruciform specimen and the loading directions with respect to the material principal directions. (a) Geometry of the specimen, (b) MD and CD coincide with the machine axes, (c) MD and CD are tilted with 45°.
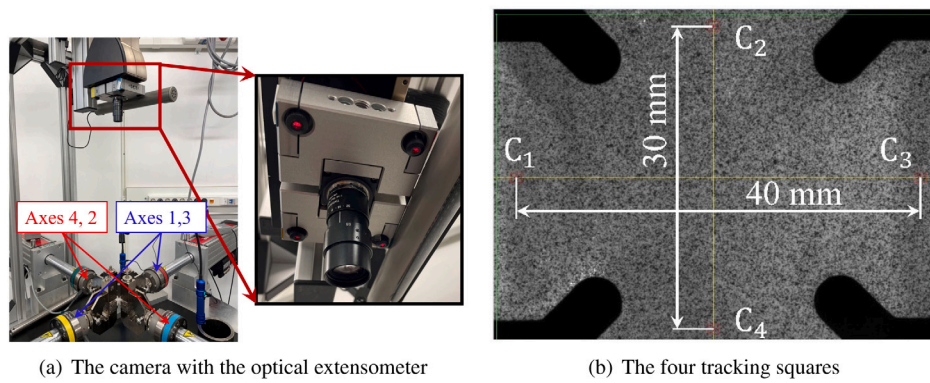

(a) The camera with the optical extensometer   (b) The four tracking squares

Fig. 2. The optical-extensometer device attached to the bi-axial test machine.

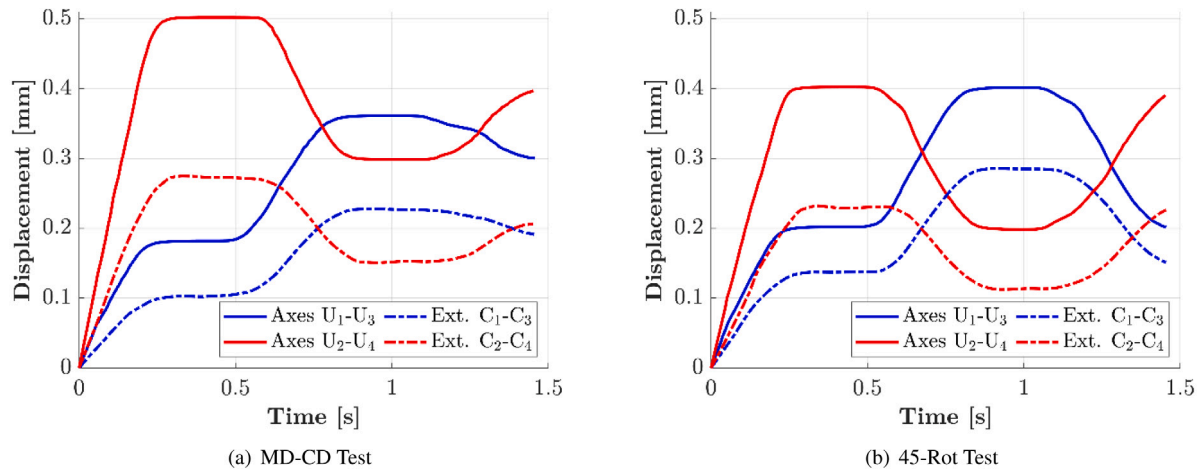(a) MD-CD Test   (b) 45-Rot Test

Fig. 3. Prescribed displacements applied to the machine axes (solid line) and the measured displacements using the optical extensometer device (dashed–dotted line).

1–3 and 2–4, respectively, are chosen to be large enough to trigger the non-linear response of the material without damaging the samples.

During the bi-axial test, there could be an influence of sliding in the clamps which can be considerable, due to the relatively high stiffness of the material, the large width and the short length of the samples. This slippage, even for a small value, can result in a large deviation between the applied and measured displacements. The applied displacements are relatively small and to minimize the measurement error, the Optical Extensometer Device (OED) is used, see Fig. 2(a). This device uses four optical markers defined on the speckle patterns of the specimen

to track the changes in the longitudinal distance and cross distance. These distances are defined between the four tracking squares, cf. Fig. 2(b).

During the test, as the axes of the machine move, the dotted area contained in each square will move due to deformation. The pattern in the squares is traced to derive the average displacement in the middle. The initial distances between the centers of extensometers tracking squares, C_1-C_3 and C_2-C_4, are less than the distance between the clamps which is 46 mm for axes 1–3 and 2–4, see Fig. 2(b). The selected distances are the maximum allowed by OED in the used machine. For
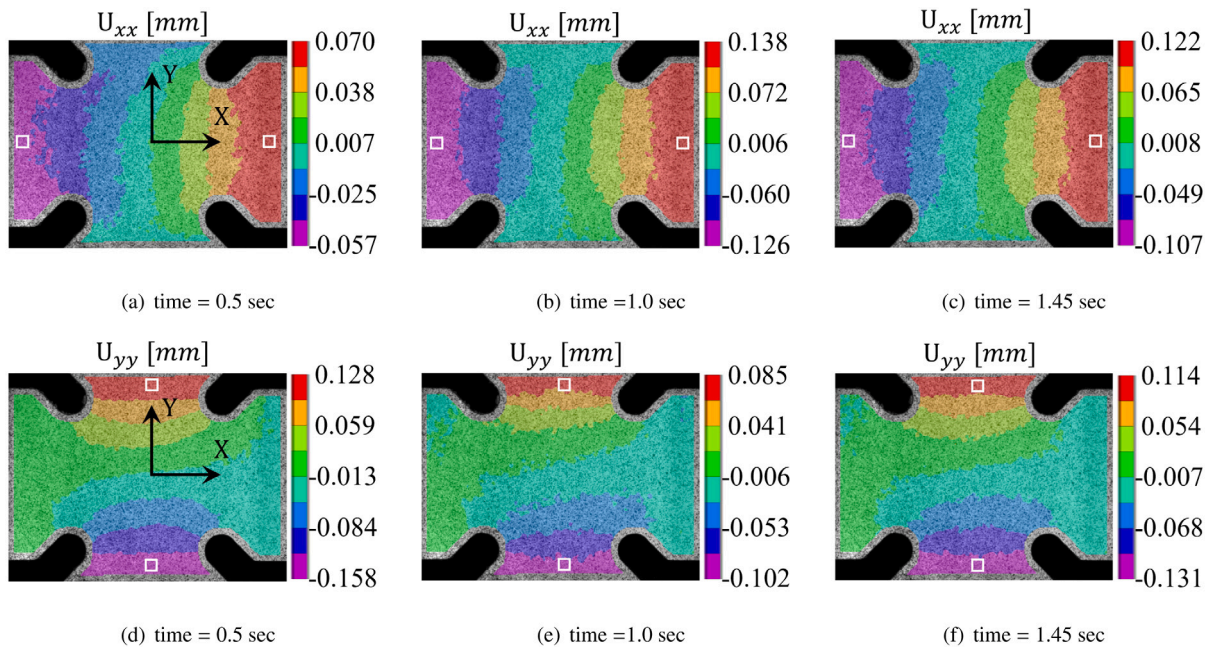
Fig. 4. Displacement fields in X and Y directions for the MD-CD test at three different load stages with OED sampling points shown by white squares.
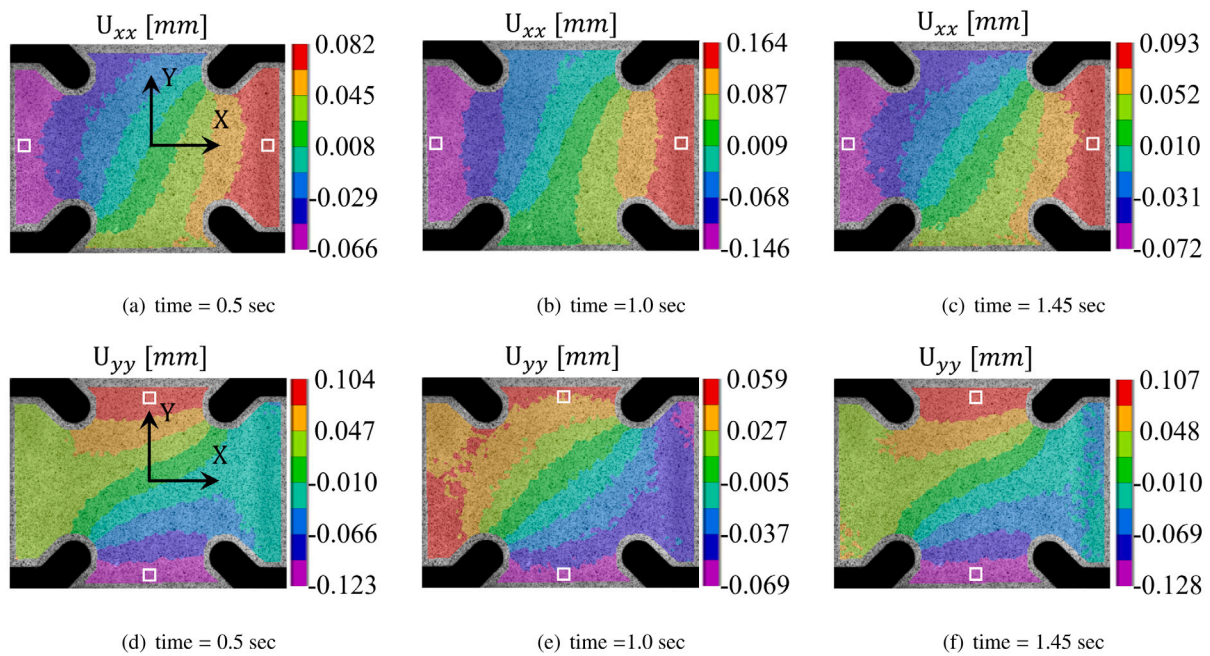

Fig. 5. Displacement fields in X and Y directions for the 45-Rot test at three different load stages with OED sampling points shown by white squares.

larger distances, the focus of the camera used by OED would be missed and the tracking would no longer be applicable.

The axes in the test move simultaneously in the opposite directions according to the prescribed displacement and no axis is fixed. Here, axes 1 and 3 move with the same magnitude in opposite directions simultaneously. The same is also applied to axes 2 and 4. This simultaneous movement is to avoid the shifting of the mid of the sample during the biaxial loading. The total axes movements and the measured displacements using the optical extensometer device are shown in Fig. 3(a) for MD-CD Test and in Fig. 3(b) for the 45-Rot Test. From Fig. 3(b), it is evident that the measured displacement using the OED for C_1-C_3 is larger than that for C_2-C_4, even though the maximum axes movement is the same for both axes U_1-U_3 and U_2-U_4. This difference is

to a large extent due to the locus of the optical tracking squares being away from the grippers. For C_1-C_3 the tracking squares are closer to the clamps compared to C_2-C_4. However, at this point, it is unclear if any sliding in the clamps took place. We will investigate this in the next section.

Furthermore, the OED does not track the full specimen, instead, it tracks the areas defined by the tracking squares and the speckled pattern within these areas. The advantage of using the OED is that it is an integrated part of the system and does not require post-processing with synchronization as opposed to the third-party Digital Image Correlation (DIC) system. Instead, it reports the measured displacement directly synchronized with the force measurements.
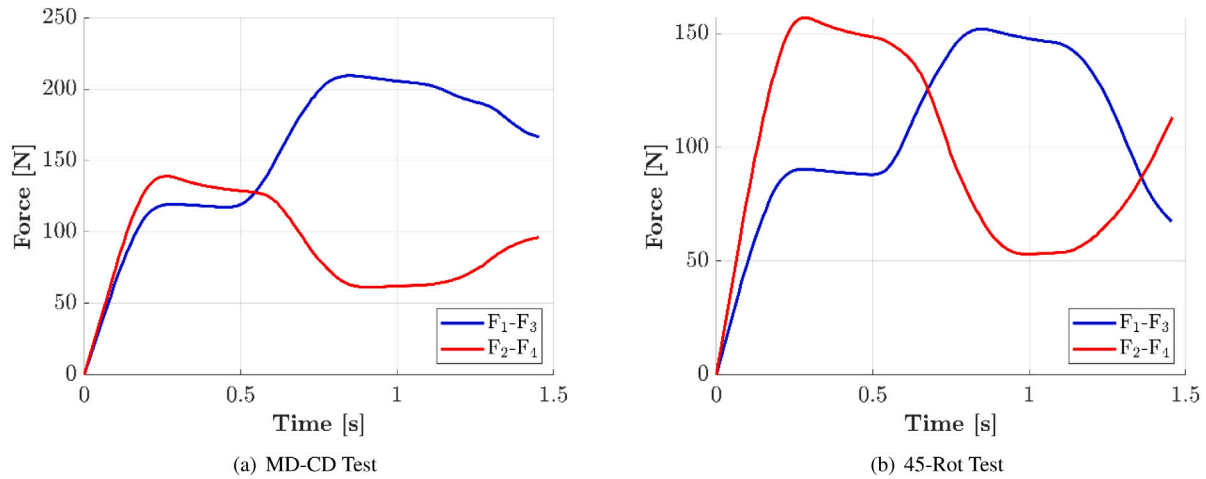
(a) MD-CD Test

(b) 45-Rot Test

Fig. 6. Measured reaction forces at different axes.

However, it is important to make sure that the displacement is sampled from the areas without large strain gradients. We used the camera system (videoXtens 1–270) of the OED and VIC-2D (VIC, 2021) software to extract the displacement fields. In Figs. 4–5, the displacement fields in X and Y directions for the MD-CD Test and 45-Rot Test are presented for three different load stages at times 0.5 s, 1.0 s, and 1.45 s. The locations of the tracking squares are also presented in Figs. 4–5 which show the results of the DIC measurements. The placement of tracking squares C_1 and C_3 are in regions with homogeneous displacement fields as they are close to the clamps. The tracking squares C_2 and C_4 are located slightly away from the clamps due to the limitations of the particular testing system but it is still in the area where the displacement field is affine.

The measured reaction forces F_1-F_3 (blue line) and F_2-F_4 (red line), from the MD-CD Test and 45-Rot Test are shown in Figs. 6(a) and (b), respectively. Comparison between the reaction forces and the applied displacements in Figs. 6 and 3, respectively, shows that the forces approximately follow the form of the applied displacements. The forces show some degree of relaxation during the period when the clamps are in the hold position.

4. Finite-element simulation

A FE model using quadratic 2D plane stress elements (Plane183 in Ansys) is employed for the simulation. Utilizing the symmetry of the MD-CD Test setup in Fig. 1, the FE-model is presented in Fig. 7. However, for the 45-Rot Test, the full geometry is used as the symmetry conditions cannot be applied. The prescribed displacements at the edges of the FE model were back-fitted so that the elements at the same locations of the four tracking squares have the same displacements as those measured by the OED. Then, in order to evaluate the amount of sliding, Figs. 8(a) and (b) show the fitted displacements in the FE model compared to the prescribed axes movements for the MD-CD Test and 45-Rot Test, respectively.

In Fig. 8(a) it is evident that the prescribed displacement U_2-U_4 (red line) in CD shows a small difference between the back-fitted displacement and the axes movements. This suggests lower slippage due to the significantly lower stiffness of the material in CD. At the same time, for the prescribed displacement U_1-U_3 (blue line), a larger difference is seen which indicates a larger amount of slippage in MD. Although the estimated slippage is below 0.1 mm, it is significant for the combination of geometry and material properties. From Fig. 8(b), the prescribed displacements U_1-U_3 and U_2-U_4 for the 45-Rot Test show similar differences between the back-fitted displacement and the axes movements. This indicates the same amount of slippage for both tested directions with a greater slippage at larger stresses. This is expected
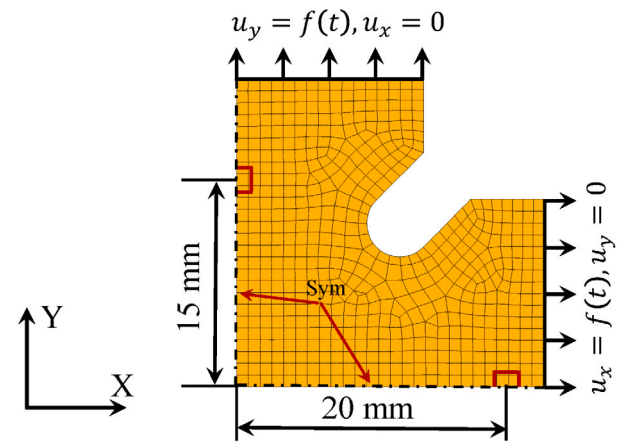

Fig. 7. The FE model used for the MD-CD Test.

as the material has the same properties in the tested directions for the 45-Rot Test. In Appendix, the numerical scheme of the implemented Ansys UMAT of the Hoffman and Xia models is outlined.

5. Material characterization

For the material characterization, uni-axial tests in MD, 45° and CD were conducted. The samples used in this work are bleached paperboard with clay coated top layer. The thickness of the material is 0.38 mm. The size of the samples is 15×100 mm^2 and the strain rate is 100 mm/min, cf. ISO-1924-3 (2005). The test was done in a climate-controlled room with 50% relative humidity and 23 °C which is a standard for testing paper materials. The average (mean) tensile test in each direction together with error bars representing the standard deviations of the experimental measurements are shown in Fig. 9. The average responses from Fig. 9 (black line) will be used to determine the elastic and plastic material parameters in the following subsection. In addition, the elastic–plastic characterization of the material is also possible using the biaxial test. However, due to the inhomogeneous spatial stress and strain field in the cruciform specimens, this procedure commonly not as straightforward as for the uniaxial case (Schemmann et al. (2018b)). This inhomogeneity in the strain and stress local fields imposes the need of inverse parameter identification (Schemmann et al. (2018a), Mahnken and Stein (1996)).
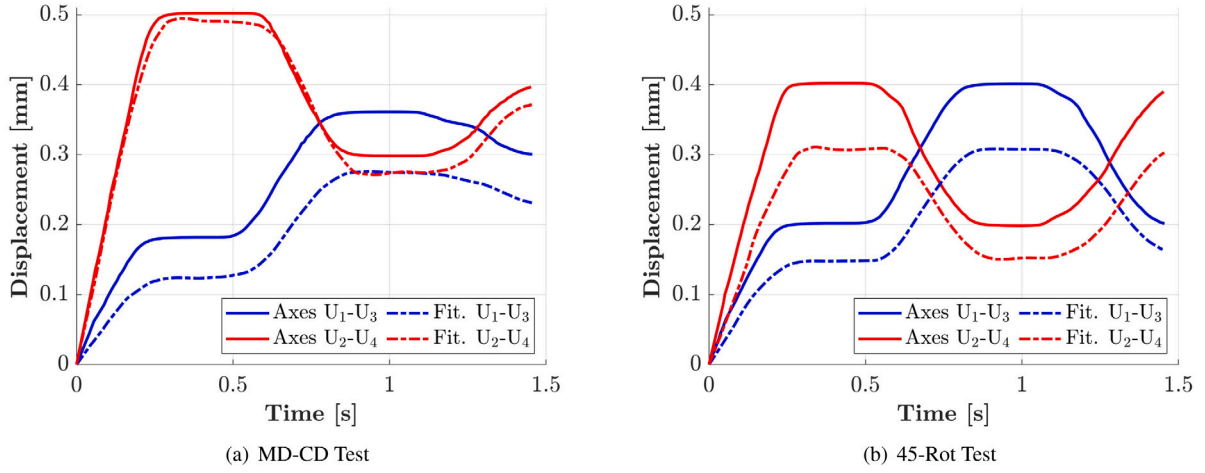
(a) MD-CD Test

(b) 45-Rot Test

Fig. 8. Prescribed displacements applied to the axes (solid line) and the applied displacements used in the FE model (dashed–dotted line).
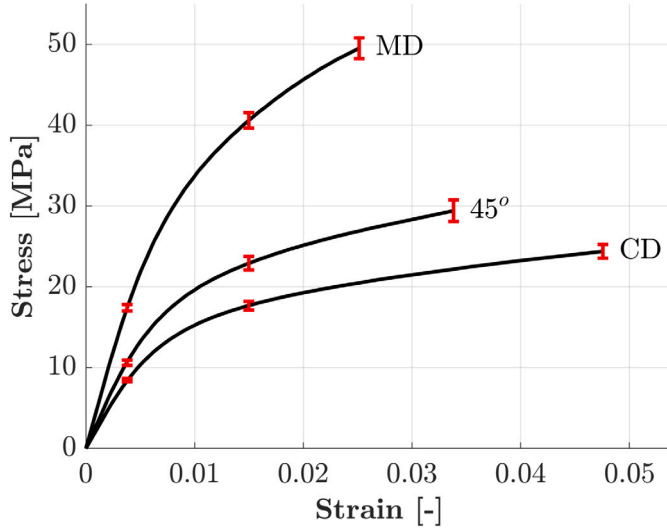

Fig. 9. The average measured uniaxial response of the material in MD, 45° and CD. Error bars show the standard deviation of the different measurements of the experiment.

Table 1
Elastic parameters.

E_{xx} [MPa]	E_{yy} [MPa]	G_{xy} [MPa]	v_{xy}
4558	2359	1105	0.40

5.1. Material properties for the Hill and Hoffman models

The material parameters needed for the calibration of the Hill and the Hoffman models are the in-plane elastic properties which represent the components of the orthotropic elastic stiffness matrix and the plastic parameters.

The elastic moduli E_{xx}, E_{45} and E_{yy} for MD, 45°, and CD, respectively, are defined at 0.02% plastic strain (i.e. at a relatively low value to preserve the smoothness of the fitting). The Poisson's ratio in turns is calculated as $v_{xy} = 0.293\sqrt{E_{xx}/E_{yy}}$ (Baum et al., 1982). The shear modulus G_{xy} is calculated as Lekhnitskii (1981)

$$G_{xy}^{-1} = 4E_{45}^{-1} - \left(E_{xx}^{-1} + E_{yy}^{-1}\right) + 2v_{xy}E_{xx}^{-1}. \tag{16}$$

where v_{xy} is the Poisson's ratio. In Table 1, the elastic parameters fitted from the experimental data in Fig. 9 are tabulated.

The plastic parameters in (3)–(5) are next to be calibrated. The hardening modulus H_0 and hardening exponent n in (5) are defined with the assumption that the CD is the equivalent direction, i.e. $R_{yy} = 1$ and setting $R_{zz} = 1$. Although R_{zz} has an influence on the yield surface even in the plane stress condition (de Souza Neto et al. (2008)), excluding it from the set of fitting parameters did not impair the fitting accuracy. The yield stress σ_0 is defined at 0.02% plastic strain. The anisotropic plastic parameters R_{xx} and R_{xy} are defined by fitting (5) to the uni-axial responses of the material. The plastic parameters in the Hill model ($q = 0$) and the Hoffman model at tension are summarized in Table 2. The corresponding fitting results are shown in Figs. 10(a) and (b), respectively.

From Table 2 it is noticed that the initial yield stresses are different. This is explained by the yield function of the Hoffman model, which differs from that of Hill with the term $q^T\sigma$, hence the yield surfaces are different. The yield stress is the result of the fitting procedure in which tests from the three directions are used simultaneously. Due to differences in the yield surfaces, the optimal yield stress may appear to be slightly different between various plasticity models. It is however noted that, in contrast to bilinear plasticity case, the effect of these differences on the reported results is minor with the non-linear hardening law used here since the curve follows smoothly the response beyond the yield limit.

5.2. Material properties of the Xia model

The elastic properties of the Xia potential are identical to the Hill and Hoffman models, cf. Table 1. However, for the plastic response, the N_γ tensors describing the gradient of the sub yield surfaces are defined based on the assumption that the plastic strain rate ratio equals to the total strain rate (Borgqvist et al. (2014)), i.e.

$$\frac{\dot{\varepsilon}_{xx}^p}{\dot{\varepsilon}_{yy}^p} = \frac{n_{11,1}}{n_{22,1}} = v_{xy} \tag{17}$$

This assumption is due to the axial and lateral strain ratio for paperboard materials remaining almost constant (Harrysson and Ristinmaa (2008), Xia et al. (2002)). Here, N_γ is of unit length such as

$$\sqrt{(n_{11,1})^2 + (n_{22,1})^2 + 2(n_{12,1})^2} = 1 \tag{18}$$

Furthermore, no coupling to shearing yields $n_{12,1} = n_{12,2} = 0$. Hence, $n_{11,1}$ and $n_{22,1}$ can be determined. A similar procedure can be used for the CD direction. The components of N_γ are tabulated in Table 3.

Since the benchmark involves bi-axial tensile tests, the characterization is limited to 3 tensile sub-surfaces. The yield stress of the hardening functions in (10) for the sub-surfaces $\gamma = 1$, 2, 3 is calculated based
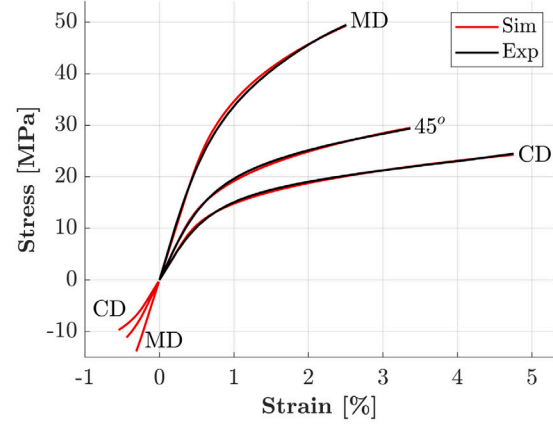
Table 2
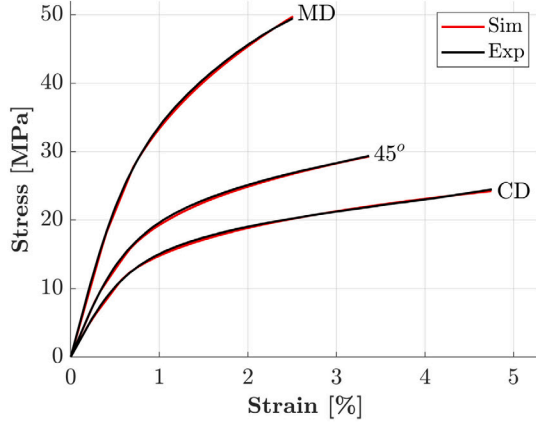Plastic parameters for the Hill and Hoffman models.

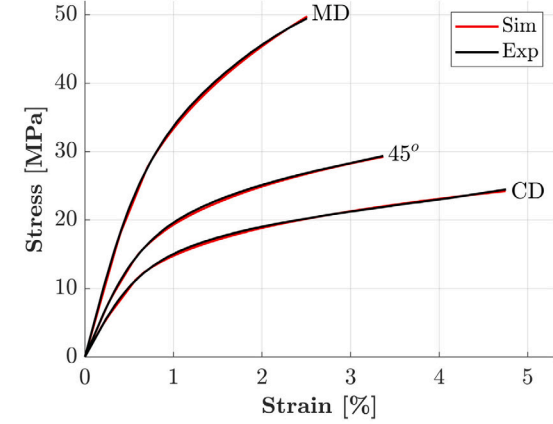| Model	σ_0 [MPa]	H_0 [MPa]	n	R_{xx}	R_{xy}	$\sigma_{xx}^{y,t} - \sigma_{xx}^{y,c}$ [MPa]	$\sigma_{yy}^{y,t} - \sigma_{yy}^{y,c}$ [MPa]
Hill	6.082	55.51	3.148	2.466	1.204	–	–
Hoffman	4.526	55.51	3.148	2.406	1.237	6.84	2.71
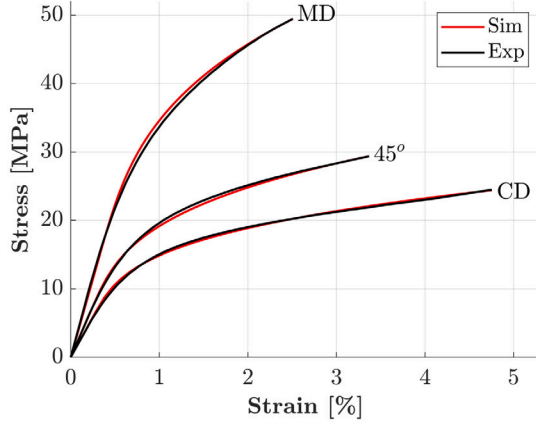
(a) Hill model calibration

(b) Hoffman model calibration

(c) Xia model calibration for $k = 1$

(d) Xia model calibration for $k = 2$

Fig. 10. Hill, Hoffman, and Xia model calibration results compared to experimental measurements.

Table 3
Components of the normal to the yield sub-surface, cf. Borgqvist et al. (2014).

Sub-surface γ	n_{11}	n_{22}	n_{12}
1	$1/\sqrt{1 + v_{xy^2}}$	$-v_{xy}/\sqrt{1 + v_{xy^2}}$	0
2	$-v_{yx}/\sqrt{1 + v_{yx^2}}$	$1/\sqrt{1 + v_{yx^2}}$	0
3	0	0	$1/\sqrt{2}$
4	-1	0	0
5	0	-1	0
6	0	0	$-1/\sqrt{2}$

on the experimental uni-axial test at 0.02% plastic strain. The internal hardening parameter κ_γ is calculated for MD and CD respectively as

$$\kappa_1 = \frac{\varepsilon_{xx}^p}{n_{11,1}} \quad \text{and} \quad \kappa_2 = \frac{\varepsilon_{yy}^p}{n_{22,2}}, \tag{19}$$

where ε_{xx}^p and ε_{yy}^p are the plastic strain in MD and CD, respectively. For $\gamma = 3$ which corresponds to positive shear, the corresponding internal hardening parameter is given by

$$\kappa_3 = S\varepsilon_{xy}^p, \tag{20}$$

where

$$S = \frac{1}{n_{12,3}} \left[1 - \left(\frac{n_{11,1} + n_{22,1}}{C_1} \right)^{2k} - \left(\frac{n_{11,2} + n_{22,2}}{C_2} \right)^{2k} \right]^{1/2k}, \tag{21}$$

where ε_{xy}^p is the plastic strain in the 45° direction. The constants C_1 and C_2 are calculated as

$$C_1 = \frac{n_{11,1}\sigma_{0,1}}{\sigma_{0,3}/2} \quad \text{and} \quad C_2 = \frac{n_{22,2}\sigma_{0,2}}{\sigma_{0,3}/2}. \tag{22}$$

The hardening functions of the sub-surfaces K_γ can be defined from experimental measurements using the plastic stresses and components of $\boldsymbol{N}_\gamma$ tensors as

$$K_1 = n_{11,1}\sigma_{xx}^p, \quad K_2 = n_{22,2}\sigma_{yy}^p \quad \text{and} \quad K_3 = \sigma_{xy}^p/S. \tag{23}$$

Also, the hardening parameters in (10) can be written as

$$K_{0,1} = n_{11,1}\sigma_{0,1}, \quad K_{0,2} = n_{22,2}\sigma_{0,2} \quad \text{and} \quad K_{0,3} = \sigma_{0,3}/S, \tag{24}$$

where $\sigma_{0,1}$, $\sigma_{0,2}$ and $\sigma_{0,3}$ are the yield stresses for sub-surfaces $\gamma = 1, 2, 3$, respectively. Finally, the hardening moduli $c_{1,\gamma}$ and hardening exponents $c_{2,\gamma}$ in (10) can be determined by a numerical fitting procedure.
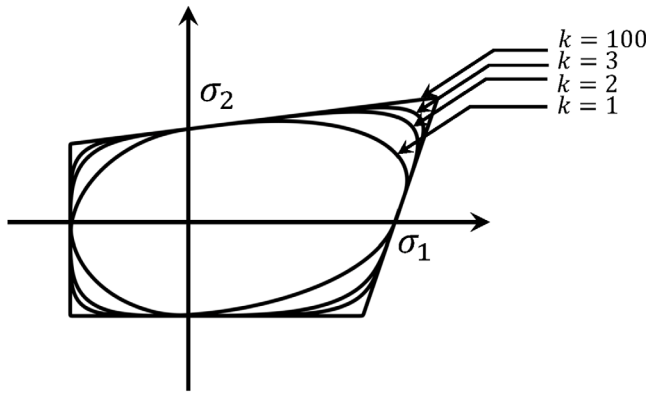
Fig. 11. The shape of the Xia yield surface for different k values.

Table 4
Plastic hardening parameters of the Xia model for different k values.

	$k = 1, 2, 3, 100$		$k = 1$	$k = 2$	$k = 3$	$k = 100$
	$\gamma = 1$	$\gamma = 2$	$\gamma = 3$	$\gamma = 3$	$\gamma = 3$	$\gamma = 3$
$K_{0,\gamma}$	16.43	5.22	7.64	5.86	5.96	5.91
$c_{1,\gamma}$	188.49	51.56	74.76	54.96	53.51	51.26
$c_{2,\gamma}$	2.295	3.258	2.84	2.93	2.84	2.84

5.2.1. Impact of the Xia shape parameter, k

From (7) it is observed that the integer k can influence the shape of the Xia yield surface. Fig. 11 shows the changes of the yield surface for different k values. Lower k values result in lower yield stresses for bi-axial loading and vice versa.

This indicates that k influences the shear sub-surface $\gamma = 3$ is dominant, meanwhile its impact on sub-surfaces $\gamma = 1, 2$ is minimal. The plastic parameters for the tensile sub-surfaces $\gamma = 1, 2, 3$ with $k = 1, 2, 3, 100$ are determined by fitting the set of Eqs. (19)–(24) to the tensile experimental data presented in Fig. 9. The plastic parameters for the Xia potential are tabulated in Table 4 for different k values. Fig. 10(c) and (d) show the fitting quality for $k = 1$ and $k = 2$, respectively. This dependency on the k value of the Xia model for bi-axial stresses suggests the need for bi-axial tests for the calibration of the model. The bi-axial FE responses (see Section 4) of the Xia model are shown in Fig. 12 for different k values, together with the recorded bi-axial forces from Fig. 6. A comparison between the simulations and experiments in Fig. 12 shows a stiffer model prediction for higher k values. To determine the k value that best fits the experimental data, the areas under the response curves for $k = 1, 2, 3, 100$ are compared to that from the experimental curves for both MD-CD Test and 45-Rot Test. For $k = 1$, the simulated bi-axial forces present the closest matching to the measured bi-axial ones. The calibrations of the Hill, Hoffman and Xia model to the uni-axial data in Figs. 10(a), (b), (c) and (d), respectively, show an excellent fitting and all models perform equally well.

5.3. Tension and compression for Hill, Hoffman, and Xia models

The asymmetric tension-compression response is featured in many materials such as composite (Lv et al. (2020)), metals (Jung et al. (2019)), and ceramic (Liu et al. (2019)). Several works aimed at addressing this behavior. Cazacu et al. (2006) introduced asymmetric orthotropic yield criterion for magnesium and titanium alloys based on the deviatoric stresses to ensure insensitivity to the hydrostatic pressure. Lee et al. (2008) used hardening law based on two surface model to study stress–strain response of Magnesium alloy sheet including the Bauschinger effect (Sowerby et al. (1979)). Using a modified Drucker–Prager yield criterion, Ryou et al. (2007) presented elasto-viscoplastic

model features asymmetric response to analysis the mechanical performance of woven composites. Based on Tsai–Wu failure criterion (Tsai and Wu (1971)), Kim et al. (2008) presented model for fiber reinforce composites to account for inelastic nonlinear response with asymmetric tension compression, later Michel and Billington (2014) extended it to account for differential hardening in compression and tension. N'souglo et al. (2019) utilized plastic orthotropic model with tension-compression asymmetry to study the formation of necking instabilities in titanium flat specimens subjected to dynamic loading. Nayebi et al. (2021) coupled von Mises criterion with isotropic continuum damage model to capture the tension-compression response of additively manufactured alloys.

Although the presented material models can represent the compressive part, the limitation of this study is the lack of verification of the compressive response. Testing the compressive behavior of such thin materials as paperboard is complicated by the dominance of geometrical buckling. This would require an additional setup for its prevention, which our group does not have at our disposal currently.

As mentioned earlier, the uni-axial experimental data are limited to the tension case only. Hence, for illustration purposes, the shape of the yield surface for the models at bi-axial compression is discussed. The compressive data of bleach board from Borgqvist et al. (2014) are utilized.

The stress–strain curves for tension-compression are shown in Fig. 10(b). The Hoffman plastic parameters at compression are tabulated in Table 2. The yield surfaces for the Hill and the Hoffman are presented in Fig. 13(a) as a blue line and a black line, respectively. A higher yield stress can be observed for the Hoffman model compared to the Hill model for the bi-axial case. This is explained by the contribution of the vector $\boldsymbol{q}$ in (4). The components of $\boldsymbol{q}$ increase the yield stress for the bi-axial case proportionally with the difference in the tension-compression response.

In Fig. 13(b) the Xia yield surface is plotted schematically as a blue solid line for both tension and compression, i.e. the compression sub-surfaces 4, 5 and 6 are equal to the tension sub-surfaces 1, 2 and 3, respectively. The black dashed line in Fig. 13(b) corresponds to a Xia yield surface where the compression sub-surface 4, 5 and 6 differ from the tension sub-surface 1, 2 and 3, respectively. Since the Xia yield surfaces are decoupled, the compression data does not influence the pure tensile sub-surfaces.

6. Results and discussion

The simulation results of the Hill, Hoffman, and Xia model (for $k = 1, 2$ and 3) are compared to the experimental measurements. The simulation and experimental results are presented for the MD-CD Test and the 45-Rot Test in Figs. 14(a) and (b), respectively. The simulated reaction forces using the Hill, Hoffman, and Xia model for $k \leq 2$ are in agreement with the experimental results. As expected, the simulated reaction forces are higher than the measured forces due to the relaxation properties of the material and the absence of viscosity in the models.

It can be observed from Figs. 14(a) and (b) that the Xia model with $k = 3$ (see Borgqvist et al. (2014)) consistently shows a stiffer response compared to the Hill and Hoffman models. Furthermore, when $k \geq 3$, it is observed that the yield occurs earlier in the Hill and Hoffman models compared to the Xia model.

For the Xia model with shape parameter $k = 2$ (Xia et al., 2002), the bi-axial response is similar to that from the Hoffman model. Also, slightly stiffer bi-axial responses can be observed for the Xia model with $k = 2$ and the Hoffman model compared to the Hill model. For the Xia and Hoffman models, this stiffer response is due to the choice of shape parameter k and to the linear term of stresses $\boldsymbol{q}^T \boldsymbol{\sigma}$ in (2), respectively. It is also noted that the difference in the yield surfaces between the Hoffman and Hill model is proportional to the tension-compression yield stresses as in (4), see Fig. 13(a).
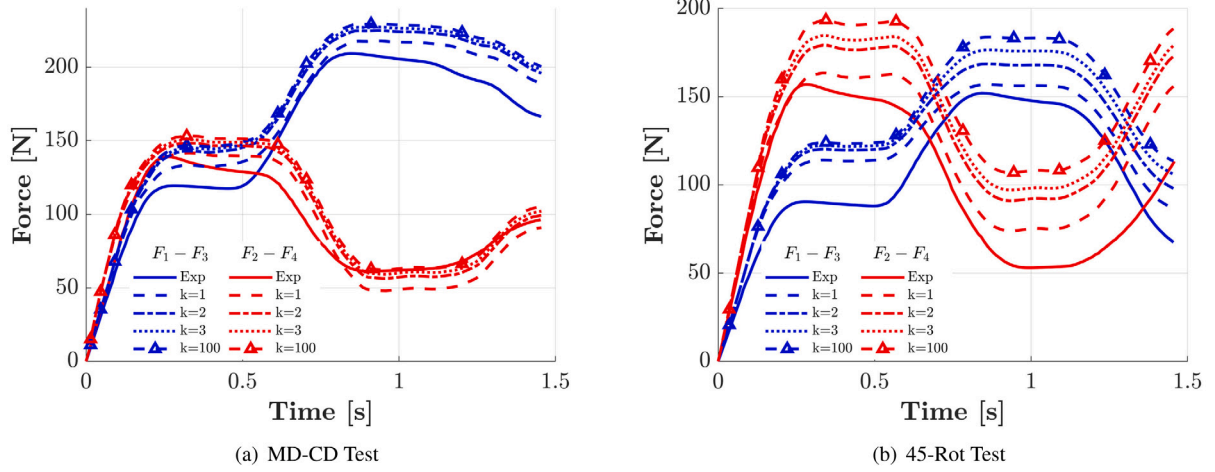
(a) MD-CD Test

(b) 45-Rot Test

Fig. 12. Bi-axial responses of the Xia model for different *k* values together with the experimental bi-axial measured forces.

(a) Yield surfaces for Hill and Hoffman model
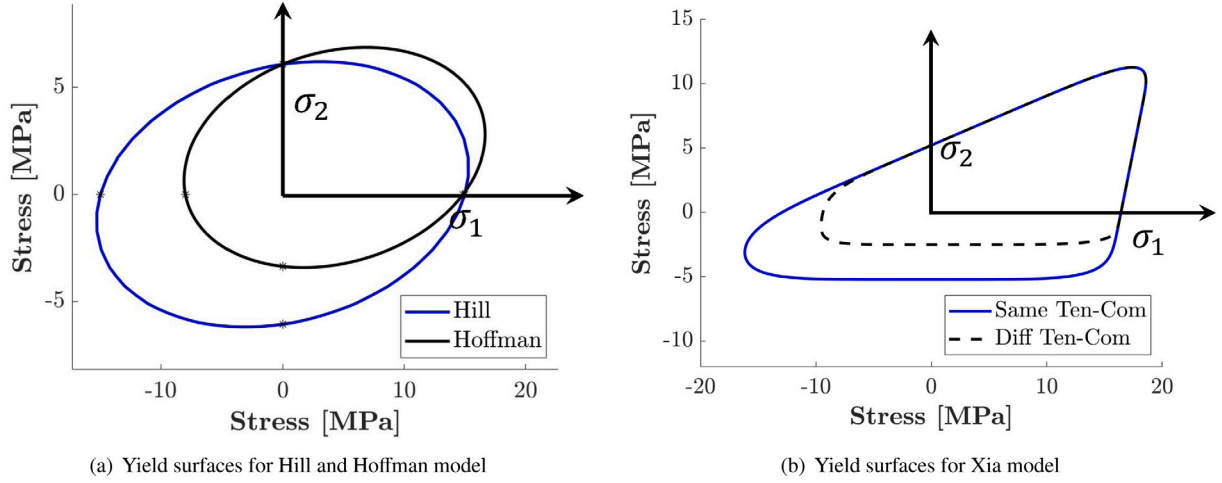
(b) Yield surfaces for Xia model

Fig. 13. The yield surfaces of the Hill, the Hoffman and the Xia model. (a) The Hill yield surface for symmetric responses and the Hoffman yield surface for asymmetric responses, (b) the Xia yield surfaces for the same tension-compression and asymmetric response.

(a) MD-CD Test

(b) 45-Rot Test
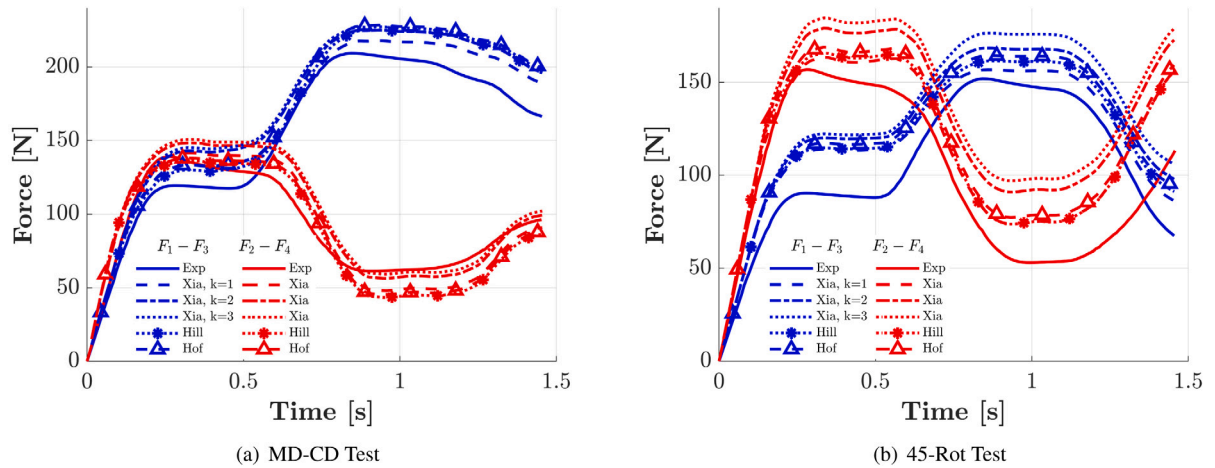
Fig. 14. Comparison of experimental measurements to the simulation results for the Hill, Hoffman, and Xia models. The Xia shape parameter $k = 1, 2,$ and 3 are used in the simulation.

In order to systematically determine the model with the best prediction, the areas under the simulated reaction curves for both MD-CD Test and 45-Rot Test are calculated for all models and compared to experiments, see Table 5. The differences between the areas defined by the experimental curves and those defined by the simulated curves are calculated for MD-CD Test and 45-Rot Test. For the Hill model, the difference between the area beneath the simulated curves for both tests and the area from the experiment is 65.20 N·sec. For the Hoffman

Table 5
Areas defined by the curves of experiment, Hill, Hoffman, and Xia for $k = 1, 2$, and 3.

	Experiment	Hill	Hoffman	Xia, $k = 1$	Xia, $k = 2$	Xia, $k = 3$
Areas of MD-CD Test, [N·sec]	358.16	373.06	380	375.62	396.19	402.49
Areas of 45-Rot Test, [N·sec]	297.76	348.06	355.96	342.25	375.44	390.01

Table 6
Summary of the comparison between the Hill, Hoffman and Xia models.

	Hill	Hoffman	Xia
Convexity	Conditionally convex depending on the orthotropic plastic matrix	Conditionally convex depending on the orthotropic plastic matrix	Unconditionally convex
Number of plastic parameters	5	7	12

model, the difference between the areas is 80.04 N·sec. For the Xia model, the differences are 61.95 N·sec, 115.71 N·sec and 136.58 N·sec for $k = 1, 2$, and 3, respectively. The Xia model with $k = 1$ followed by the Hill model present the closest results to the experiments. The Hoffman and Xia model with $k = 2$ show slightly stiffer responses compared to the experiment with a closer response of Hoffman to the experiment compared to Xia with $k = 2$. Meanwhile, the Xia model with $k \geq 3$ shows a stiffer response and the deviation is greater compared to the other models.

In terms of the number of material parameters, the Hill and Hoffman models require five and seven plastic parameters, respectively, cf. Table 2. The complexity of the Xia model is greater, requiring a minimum of twelve plastic parameters: one parameter describing the shape of the yield surface, nine parameters describing the hardening rule, cf. Table 4, and two parameters describing the compression behavior (assuming perfect plasticity for the compressive part), cf. Borgqvist et al. (2014). The unit vectors N_γ controlling the direction of the sub-surface, cf. Table 3, are excluded in the counting of plastic parameters, since the direction is given by the Poisson's ratio v_{xy}. The greater number of parameters gives the Xia model a better ability to characterize the material. For each loading direction there are separate parameters for yield stress, hardening modulus and hardening exponent. Meanwhile, for the Hoffman model, these plastic parameters are defined for only one loading direction. By using the components of the orthotropic plastic matrix P, these components are used to match the response of the experiment and may not always yield a good fit.

7. Conclusion

In this work, bi-axial tension experiments are conducted using cruciform specimens with the material principal directions coinciding with the machine axes as well as with the samples tilted by 45 degrees. The results from the experiments are compared with FE simulations using three elasto-plastic continuum models. The first two are based on the Hoffman criterion while the third model is based on the Xia yield criterion. The Hoffman and Xia models are able to replicate the pressure sensitivity and anisotropic properties of the fibrous materials. Their implementations, which are not available in commercial software, are provided with the publication together with the complementary fitting tool for the Xia model.

The comparison between the models and experiments showed that Xia with $k = 1$, followed by Hill, present the closest responses to the experiments. This result suggests that for the case with a symmetric tension-compression response, the Hill model is able to capture adequately the mechanical response of the material for bi-axial loading conditions. For the Hoffman and the Xia model with $k = 2$, the closest response to the experiment is presented by Hoffman compared to Xia with $k = 2$. But both models show slightly stiffer responses with respect to the measured bi-axial responses. Meanwhile, for the Xia $k \geq 3$ the bi-axial response is stiffer and the simulated forces deviate from that for the experiment.

The Xia model has more flexibility in fitting the material properties due to the larger number of material properties and versatile yield functions. However, this study shed the light on the importance of calibrating the k parameters of the Xia model, as for $k \geq 3$ values a stiffer bi-axial response is presented. This requirement of bi-axial tests for Xia calibration can be a cumbersome task.

In terms of stability, the Xia yield surface is unconditionally convex while the Hill and Hoffman yield surfaces are conditionally convex depending on the components of the orthotropic plastic matrix P. However, in the present study, the advantage was not substantial.

As opposed to the Hill model, the Hoffman model features a different tension-compression response by changing the shape of the yield surface. This change in the shape of the yield surface requires re-calibration of both tension and compression responses. However, for the Xia model, the difference in tension-compression does not influence the tensile sub-surfaces and only the compressive sub-surfaces require calibration. A summary of the comparison between the Hoffman and the Xia model is presented in Table 6.

The conducted experimental study also shows the importance of accounting for slippage at the grippers for the accurate testing and comparison against the experiments in the bi-axial testing, where the used samples are wider and shorter than that used in uniaxial measurements. It also indicated the importance of viscoelasticity as the observable relaxation was recorded in the experiments even with relatively fast loading rates.

8. Code availability

The UMAT implementations of Hoffman and Xia models for Ansys and Abaqus together with Matlab calibration tool for the Xia model are available at https://doi.org/10.5281/zenodo.5777175.

Declaration of competing interest

The authors declare that they have no known competing financial interests or personal relationships that could have appeared to influence the work reported in this paper.
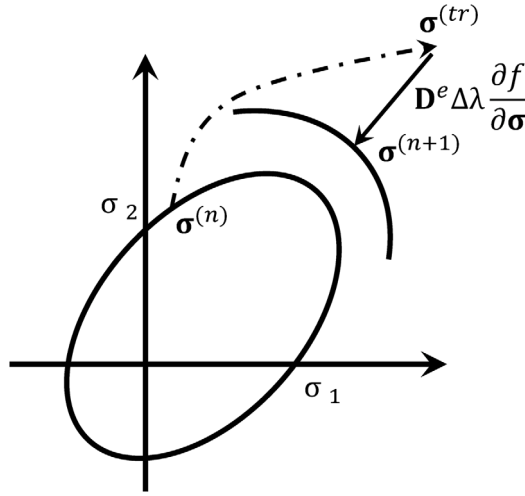
Acknowledgments

Fig. A.1. Radial return mapping algorithm.

Appendix. Numerical scheme

The numerical scheme outlined in this section is implemented into a user material routine (UMAT) using the general-purpose FE program Ansys.

The relation between stress vector, $\boldsymbol{\sigma} = \left[\sigma_{xx}, \sigma_{yy}, \sigma_{xy}\right]^T$, and the elastic strain vector, $\boldsymbol{\varepsilon}^e = [\varepsilon_{xx}^e, \varepsilon_{yy}^e, \varepsilon_{xy}^e]^T$, is given as

$$\boldsymbol{\sigma} = \boldsymbol{D}^e \boldsymbol{\varepsilon}^e, \tag{A.1}$$

where the orthotropic elastic stiffness matrix is given by

$$\boldsymbol{D}^e = \frac{1}{\left(1 - \nu_{xy}\nu_{yx}\right)} \begin{bmatrix} E_{xx} & \nu_{yx}E_{xx} & 0 \\ \nu_{xy}E_{yy} & E_{yy} & 0 \\ 0 & 0 & G_{xy}\left(1 - \nu_{xy}\nu_{yx}\right) \end{bmatrix}. \tag{A.2}$$

The total strain is the sum of the elastic and plastic strain, i.e. $\boldsymbol{\varepsilon} = \boldsymbol{\varepsilon}^e + \boldsymbol{\varepsilon}^p$, which inserted into (A.1) yields

$$\boldsymbol{\sigma} = \boldsymbol{D}^e \left(\boldsymbol{\varepsilon} - \boldsymbol{\varepsilon}^p\right). \tag{A.3}$$

The incremental form of (A.3) is given as

$$\Delta\boldsymbol{\sigma} = \boldsymbol{D}^e \left(\Delta\boldsymbol{\varepsilon} - \Delta\boldsymbol{\varepsilon}^p\right), \tag{A.4}$$

when $\boldsymbol{D}^e$ is a constant.

A.1. Radial return method

The yield functions (1) for Hoffman and (7) for Xia are evaluated for each strain increment $\Delta\boldsymbol{\varepsilon}$. If $f \leq 0$ then the increment is elastic, else the plastic deformation occurs and the radial return algorithm should be used to fulfill the Karush-Kuhn–Tucker conditions (Simo and Hughes (2006)) as

$$\dot{\lambda} \geq 0, \quad f \leq 0, \quad \lambda f = 0. \tag{A.5}$$

The incremental plastic strain vector, $\Delta\boldsymbol{\varepsilon}^p$, and the incremental internal hardening vector, $\Delta\boldsymbol{\kappa}$, are given as, cf. Ottosen and Ristinmaa (2005),

$$\Delta\boldsymbol{\varepsilon}^p = \int_{\lambda^{(n)}}^{\lambda^{(n+1)}} \frac{\partial f}{\partial \boldsymbol{\sigma}} d\lambda \quad \text{and} \quad \Delta\boldsymbol{\kappa} = -\int_{\lambda^{(n)}}^{\lambda^{(n+1)}} \frac{\partial f}{\partial \boldsymbol{K}} d\lambda, \tag{A.6}$$

where $\lambda^{(n+1)} = \lambda^{(n)} + \Delta\lambda$ and $\Delta\lambda$ is the incremental plastic multiplier. The superscript $(n+1)$ refers to the current integration step and the superscript (n) refers to the last integration step. Using Euler backward scheme on (A.6) gives

$$\Delta\boldsymbol{\varepsilon}^p = \frac{\partial f}{\partial \boldsymbol{\sigma}} \Delta\lambda \quad \text{and} \quad \Delta\boldsymbol{\kappa} = -\frac{\partial f}{\partial \boldsymbol{K}} \Delta\lambda, \tag{A.7}$$

where $\partial f/\partial\boldsymbol{\sigma} = (\partial f/\partial\boldsymbol{\sigma})^{(n+1)}$ and $\partial f/\partial\boldsymbol{K} = (\partial f/\partial\boldsymbol{K})^{(n+1)}$ are evaluated at the current increment, $(n+1)$.

Inserting the plastic strain increment in (A.7) into (A.4) and using $\boldsymbol{\sigma}^{(n+1)} = \boldsymbol{\sigma}^{(n)} + \Delta\boldsymbol{\sigma}$, gives

$$\boldsymbol{\sigma}^{(n+1)} = \boldsymbol{\sigma}^{(tr)} - \boldsymbol{D}^e \frac{\partial f}{\partial \boldsymbol{\sigma}} \Delta\lambda, \tag{A.8}$$

where $\boldsymbol{\sigma}^{(tr)}$ is the trial stress given by

$$\boldsymbol{\sigma}^{(tr)} = \boldsymbol{\sigma}^{(n)} + \boldsymbol{D}^e \Delta\boldsymbol{\varepsilon} \tag{A.9}$$

and $\boldsymbol{\sigma}^{(n)}$ is the stress from the last integration step.

Fig. A.1 illustrates graphically the radial return mapping algorithm derived in (A.8), where the stress from the last integration step, $\boldsymbol{\sigma}^{(n)}$, is updated into the current integration step, $\boldsymbol{\sigma}^{(n+1)}$, using the Euler backward scheme. The radial return algorithm assumes elastic strain increment, and the current step is defined once the consistency conditions are fulfilled, Ottosen and Ristinmaa (2005).

The residuals in stresses are defined using (A.8) as

$$\boldsymbol{R}_{\boldsymbol{\sigma}} = \boldsymbol{\sigma}^{(n+1)} + \Delta\lambda \boldsymbol{D}^e \frac{\partial f}{\partial \boldsymbol{\sigma}} - \boldsymbol{\sigma}^{(tr)}. \tag{A.10}$$

Similarly, the residuals in the hardening function are introduced as

$$\boldsymbol{R}_K = \boldsymbol{K}^{(n)} - \boldsymbol{K}^{(n+1)}\left(\boldsymbol{\kappa}^{(n+1)}\right), \tag{A.11}$$

where $\boldsymbol{K}^{(n)}$ is a variable and $\boldsymbol{K}^{(n+1)}$ is a function. The residual in the yield function from (7) is defined as

$$R_f = f\left(\boldsymbol{\sigma}, \boldsymbol{K}\right). \tag{A.12}$$

The residual vector $\boldsymbol{R} = [\boldsymbol{R}_{\boldsymbol{\sigma}}, \boldsymbol{R}_{K_\gamma}, R_f]^T$ is a function of the state variables $\boldsymbol{S} = [\boldsymbol{\sigma}, \boldsymbol{K}, \Delta\lambda]^T$. The solution to the non-linear set of equations $\boldsymbol{R}(\boldsymbol{S}) = \boldsymbol{0}$ is found iteratively using the Newton–Raphson method according to

$$\boldsymbol{S}^{i+1} = \boldsymbol{S}^i - \left(\frac{\partial \boldsymbol{R}}{\partial \boldsymbol{S}}\right)\boldsymbol{R}\bigg|^i, \tag{A.13}$$

with a specified tolerance on $\|\boldsymbol{R}\| = \sqrt{\boldsymbol{R}^T\boldsymbol{R}}$ and where i is the iteration number.

A.2. The algorithmic tangent stiffness matrix

For implicit solver, the tangential stiffness matrix is needed. Herein, to achieve quadratic convergence, the algorithmic tangent stiffness matrix is introduced. Inserting (A.9) in (A.10) and taking the derivatives with respect to time yields

$$\dot{\boldsymbol{\sigma}} + \dot{\lambda}\boldsymbol{D}^e \frac{\partial f}{\partial \boldsymbol{\sigma}} + \Delta\lambda\boldsymbol{D}^e \frac{\partial^2 f}{\partial \boldsymbol{\sigma}^2}\dot{\boldsymbol{\sigma}} - \boldsymbol{D}^e\dot{\boldsymbol{\varepsilon}} = 0, \tag{A.14}$$

where superscript $n+1$ have been omitted for simplicity. Rearrangement of (A.14) gives

$$\dot{\boldsymbol{\sigma}} = \boldsymbol{A}\left(\dot{\boldsymbol{\varepsilon}} - \dot{\lambda}\frac{\partial f}{\partial \boldsymbol{\sigma}}\right), \tag{A.15}$$

where

$$\boldsymbol{A} = \left[(\boldsymbol{D}^e)^{-1} + \Delta\lambda\frac{\partial^2 f}{\partial \boldsymbol{\sigma}^2}\right]^{-1}. \tag{A.16}$$

Taking the time derivative of $f(\boldsymbol{\sigma}, \boldsymbol{K}) = 0$ in (A.12) gives

$$\left(\frac{\partial f}{\partial \boldsymbol{\sigma}}\right)^T \dot{\boldsymbol{\sigma}} + \left(\frac{\partial f}{\partial \boldsymbol{K}}\right)^T \dot{\boldsymbol{K}} = 0, \tag{A.17}$$

where

$$\dot{\boldsymbol{K}} = \frac{\partial \boldsymbol{K}}{\partial \boldsymbol{\kappa}}\dot{\boldsymbol{\kappa}}. \tag{A.18}$$

The time derivative of the incremental internal hardening $\Delta\boldsymbol{\kappa}$ in (A.7) can be written as,

$$\dot{\boldsymbol{\kappa}} = -\dot{\lambda}\frac{\partial f}{\partial \boldsymbol{K}} - \Delta\lambda\frac{\partial^2 f}{\partial \boldsymbol{K}^2}\dot{\boldsymbol{K}}, \tag{A.19}$$

where it is assumed that the yield function f has mixed derivatives equal to zero, i.e. $\partial^2 f / \partial K \partial \sigma = \mathbf{0}$. Inserting (A.19) into (A.18) yields

$$\dot{K} = -H\dot{\lambda}, \tag{A.20}$$

where

$$H = \left(I + \Delta\lambda \frac{\partial K}{\partial \kappa} \frac{\partial^2 f}{\partial K^2} \right)^{-1} \tag{A.21}$$

and I is the identity matrix.

Substituting (A.15) and (A.20) into (A.17) and solving for the rate of plastic multiplier $\dot{\lambda}$, yields

$$\dot{\lambda} = \frac{1}{b} \left(\frac{\partial f}{\partial \sigma} \right)^T A \dot{\varepsilon}, \tag{A.22}$$

where

$$b = \left(\frac{\partial f}{\partial \sigma} \right)^T A \frac{\partial f}{\partial \sigma} - \left(\frac{\partial f}{\partial K} \right)^T H. \tag{A.23}$$

Inserting (A.22) into (A.15) yields the algorithmic tangent stiffness matrix D_{ats} as

$$\dot{\sigma} = D_{ats} \dot{\varepsilon}, \tag{A.24}$$

where

$$D_{ats} = A - \frac{1}{b} A \frac{\partial f}{\partial \sigma} \left(\frac{\partial f}{\partial \sigma} \right)^T A. \tag{A.25}$$

A.3. Hoffman yield surface

The numerical schemes in Appendices A.1 and A.2 are adopted to the Hoffman model presented in Sections 2.1 and 2.3 .

The Hoffman yield function in (1) is given using (2) as

$$f = \frac{1}{2} \sigma^T P \sigma + q^T \sigma - \sigma_y^2(\kappa). \tag{A.26}$$

The first and second-order derivative of (A.26) with respect to the stress are given as

$$\frac{\partial f}{\partial \sigma} = P\sigma + q^T \qquad \text{and} \qquad \frac{\partial^2 f}{\partial \sigma^2} = P . \tag{A.27}$$

The derivatives with respect to $\sigma_y(\kappa)$ are given as

$$\frac{\partial f}{\partial \sigma_y} = -2\sigma_y \qquad \text{and} \qquad \frac{\partial^2 f}{\partial \sigma_y^2} = -2. \tag{A.28}$$

By virtue of (A.8) and (A.27), the current stress $\sigma^{(n+1)}$ is written as a function of the incremental plastic multiplier $\Delta\lambda$ as

$$\sigma^{(n+1)}(\Delta\lambda) = \sigma^{(tr)} - \Delta\lambda D^e \left[P\sigma(\Delta\lambda) + q^T \right]. \tag{A.29}$$

Inserting the expression of the current stress in (A.29) into the Hoffman yield function in (A.26) and using (5) yields

$$f(\Delta\lambda) = \frac{1}{2} (\sigma(\Delta\lambda))^T P\sigma(\Delta\lambda) + \sigma(\Delta\lambda) q^T - (\sigma_0 + K(\varepsilon_{eqv}^p (\Delta\lambda)))^2. \tag{A.30}$$

The Newton–Raphson iteration are used to update the incremental plastic strain $\Delta\lambda$ as

$$\Delta\lambda^{i+1} = \Delta\lambda^i - \left(\frac{\partial f}{\partial (\Delta\lambda)} \right)^{-1} f(\Delta\lambda) \bigg|^i . \tag{A.31}$$

The iteration starts for $\Delta\lambda = 0$ and ends when the loading function in (1) is less than a specified tolerance.

A.4. Xia yield surface

The numerical schemes in Appendices A.1 and A.2 are directly applied to the Xia model presented in Sections 2.2 and 2.3 .

References

Abu-Farha, F., Hector, L., Khraisheh, M., 2009. Cruciform-shaped specimens for elevated temperature biaxial testing of lightweight materials. JOM 61, 48–56. http://dx.doi.org/10.1007/s11837-009-0121-8.

Alzweighi, M., Mansour, R., Lahti, J., Hirn, U., Kulachenko, A., 2021. The influence of structural variations on the constitutive response and strain variations in thin fibrous materials. Acta Mater. 203, 116460. http://dx.doi.org/10.1016/j.actamat.2020.11.003.

Åström, J.A., Niskanen, K.J., 1993. Symmetry-breaking fracture in random fibre networks. Europhys. Lett. (EPL) 21 (5), 557–562. http://dx.doi.org/10.1209/0295-5075/21/5/009.

Awais, M., Sorvari, J., Tanninen, P., Leppänen, T., 2017. Finite element analysis of the press forming process. Int. J. Mech. Sci. 131, http://dx.doi.org/10.1016/j.ijmecsci.2017.07.053.

Baptista, R., Claudio, R., Reis, L., Madeira, J., Guelho, I., Freitas, M., 2015. Optimization of cruciform specimens for biaxial fatigue loading with direct multi search. Theor. Appl. Fract. Mech. 80, 65–72. http://dx.doi.org/10.1016/j.tafmec.2015.06.009, 1st Multi-lateral workshop on Fracture and Structural Integrity related issues.

Baum, G.A., Habeger Jr., C.C., Fleischman Jr., E.H., 1982. Measurement of the orthotropic elastic constants of paper. Appleton, Wisconsin: the Institute,.

Beex, L., Peerlings, R., 2009. An experimental and computational study of laminated paperboard creasing and folding. Int. J. Solids Struct. 46 (24), 4192–4207. http://dx.doi.org/10.1016/j.ijsolstr.2009.08.012.

Bilko, P., Małyszko, L., 2020. An orthotropic elastic-plastic constitutive model for masonry walls. Materials 13 (18), URL https://www.mdpi.com/1996-1944/13/18/4064.

Borgqvist, E., Lindström, T., Tryding, J., Wallin, M., Ristinmaa, M., 2014. Distortional hardening plasticity model for paperboard. Int. J. Solids Struct. 51 (13), 2411–2423. http://dx.doi.org/10.1016/j.ijsolstr.2014.03.013.

Borgqvist, E., Wallin, M., Ristinmaa, M., Tryding, J., 2015. An anisotropic in-plane and out-of-plane elasto-plastic continuum model for paperboard. Compos. Struct. 126, 184–195. http://dx.doi.org/10.1016/j.compstruct.2015.02.067.

Brandberg, A., Kulachenko, A., 2020. Compression failure in dense non-woven fiber networks. Cellulose 27, 6065–6082. http://dx.doi.org/10.1007/s10570-020-03153-2.

Cazacu, O., Plunkett, B., Barlat, F., 2006. Orthotropic yield criterion for hexagonal closed packed metals. Int. J. Plast. 22 (7), 1171–1194.

Considine, J., Pierron, F., Turner, K., 2014. General anisotropy identification of paperboard with virtual fields method. Exp. Mech. 54, 1395–1410. http://dx.doi.org/10.1007/s11340-014-9903-1.

de Souza Neto, E.A., Peric, D., Owen, D.R., 2008. Computational Methods for Plasticity. John Wiley & Sons, Ltd.

Drucker, D.C., 1963. On the Postulate of Stability of Material in the Mechanics of Continua. Division of Engineering, Brown University.

Dunne, F., Petrinic, N., 2005. Introduction to Computational Plasticity. Oxford University Press on Demand.

Hägglund, R., Isaksson, P., 2008. On the coupling between macroscopic material degradation and interfiber bond fracture in an idealized fiber network. Int. J. Solids Struct. 45 (3), 868–878. http://dx.doi.org/10.1016/j.ijsolstr.2007.09.011.

Hagman, A., Nygårds, M., 2017. Thermographical analysis of paper during tensile testing and comparison to digital image correlation. Exp. Mech. 57, 325–339. http://dx.doi.org/10.1007/s11340-016-0240-4.

Hannon, A., Tiernan, P., 2008. A review of planar biaxial tensile test systems for sheet metal. J. Mater Process. Technol. 198 (1), 1–13. http://dx.doi.org/10.1016/j.jmatprotec.2007.10.015.

Harrysson, A., Ristinmaa, M., 2008. Large strain elasto-plastic model of paper and corrugated board. Int. J. Solids Struct. 45 (11–12), 3334–3352.

Heyden, S., 2000. Network modelling for evaluation of mechanical properties of cellulose fibre fluff. (Ph.D. thesis). In: Report TVSM, 1011, Lund University, Susanne Heyden, Division of Structural Mechanics, Box 118, 221 00 Lund, Sweden,, https://lup.lub.lu.se/record/19648.

Hill, R., 1948. A theory of the yielding and plastic flow of anisotropic metals. Proc. Royal Soc. Lond. Ser. A. Math. Phys. Sci. 193 (1033), 281–297. http://dx.doi.org/10.1098/rspa.1948.0045.

Hoffman, O., 1967. The brittle strength of orthotropic materials. J. Compos. Mater. 1 (2), 200–206. http://dx.doi.org/10.1177/002199836700100210.

Holzapfel, G.A., 2002. Nonlinear Solid Mechanics: A Continuum Approach for Engineering. John Wiley & Sons, Inc., ISBN: 978-0-471-82319-3.

Hristopulos, D.T., Uesaka, T., 2004. Structural disorder effects on the tensile strength distribution of heterogeneous brittle materials with emphasis on fiber networks. Phys. Rev. B 70, 064108, URL https://link.aps.org/doi/10.1103/PhysRevB.70.064108.

Hu, J.-J., Chen, G.-W., Liu, Y.-C., Hsu, S.-S., 2014. Influence of specimen geometry on the estimation of the planar biaxial mechanical properties of cruciform specimens. Exp. Mech. 54, 615–631. http://dx.doi.org/10.1007/s11340-013-9826-2.

Hu, Z., Mansour, R., Olsson, M., Du, X., 2021. Second-order reliability methods: a review and comparative study. Struct Multidisc Optim 64, 3233–3263. http://dx.doi.org/10.1007/s00158-021-03013-y.

Huang, H., Hagman, A., Nygårds, M., 2014. Quasi static analysis of creasing and folding for three paperboards. Mech. Mater. 69 (1), 11–34. http://dx.doi.org/10.1016/j.mechmat.2013.09.016.

Isaksson, P., Hägglund, R., 2007. Evolution of bond fractures in a randomly distributed fiber network. Int. J. Solids Struct. 44 (18), 6135–6147. http://dx.doi.org/10.1016/j.ijsolstr.2007.02.013.

ISO-1924-3, 2005. Paper and board - determination of tensile properties - part 3: Constant rate of elongation method (100 mm/min). BS ISO 1924-3.

Jung, J., Hur, Y.C., Jun, S., Lee, H.-S., Kim, B.-M., Kim, J.H., 2019. Constitutive modeling of asymmetric hardening behavior of transformation-induced plasticity steels. Int. J. Automot. Technol. 20 (1), 19–30.

Jungstedt, E., Montanari, C., Östlund, S., Berglund, L., 2020. Mechanical properties of transparent high strength biocomposites from delignified wood veneer. Composites A 133, 105853. http://dx.doi.org/10.1016/j.compositesa.2020.105853.

Justusson, J.W., Phillips, A., 1966. Stability and convexity in plasticity. Acta Mech. 2, 251–267. http://dx.doi.org/10.1007/BF01178866.

Kim, J.H., Lee, M.-G., Ryou, H., Chung, K., Youn, J.R., Kang, T.J., 2008. Development of nonlinear constitutive laws for anisotropic and asymmetric fiber reinforced composites. Polym. Compos. 29 (2), 216–228.

Kiriyama, K., Zhang, S., Hayashida, H., ichi Suzuki, J., Kuwabara, T., 2019. Development of a biaxial tensile testing machine for pulsed neutron experiments. MethodsX 6, 2166–2175. http://dx.doi.org/10.1016/j.mex.2019.08.015.

Kulachenko, A., Uesaka, T., 2012. Direct simulations of fiber network deformation and failure. Mech. Mater. 51, 1–14. http://dx.doi.org/10.1016/j.mechmat.2012.03.010.

Lahti, J., Dauer, M., Keller, D., Hirn, U., 2020. Identifying the weak spots in packaging paper: local variations in grammage, fiber orientation and density and the resulting local strain and failure under load. Cellulose 27, 1–17. http://dx.doi.org/10.1007/s10570-020-03493-z.

Lee, M.-G., Wagoner, R., Lee, J., Chung, K., Kim, H., 2008. Constitutive modeling for anisotropic/asymmetric hardening behavior of magnesium alloy sheets. Int. J. Plast. 24 (4), 545–582.

Lekhnitskii, S., 1981. Theory of Elasticity of an Anisotropic Body. Mir Publishers.

Li, Y., Stapleton, S.E., Reese, S., Simon, J.-W., 2016. Anisotropic elastic-plastic deformation of paper: In-plane model. Int. J. Solids Struct. 100, 286–296.

Li, H., Zhao, H., Luo, C., Li, L., Zhang, H., 2017. Research on design and simulation of biaxial tensile-bending complex mechanical performance test apparatus. Micromachines 8, http://dx.doi.org/10.3390/mi8090286.

Liu, H., Yang, Z., Yuan, H., 2019. A novel elastoplastic constitutive model for woven oxide/oxide ceramic matrix composites with anisotropic hardening. Compos. Struct. 229, 111420.

Lv, J., Xiao, Y., Zhou, Y., Xie, Y., 2020. Characterization and modeling of the creep behavior of fiber composites with tension and compression asymmetry. Int. J. Mech. Sci. 170, 105340.

Mahnken, R., Stein, E., 1996. A unified approach for parameter identification of inelastic material models in the frame of the finite element method. Comput. Methods Appl. Mech. Engrg. 136 (3–4), 225–258.

Mäkelä, P., Östlund, S., 2003. Orthotropic elastic–plastic material model for paper materials. Int. J. Solids Struct. 40 (21), 5599–5620. http://dx.doi.org/10.1016/S0020-7683(03)00318-4.

Mansour, R., Kulachenko, A., Chen, W., Olsson, M., 2019. Stochastic constitutive model of isotropic thin fiber networks based on stochastic volume elements. Materials 12, 538. http://dx.doi.org/10.3390/ma12030538.

Michel, A., Billington, S., 2014. Nonlinear constitutive model for anisotropic biobased composite materials. J. Eng. Mech. 140 (11), 04014083.

Nayebi, A., Rokhgireh, H., Araghi, M., Mohammadi, M., 2021. Modelling the asymmetric tension–compression properties of additively manufactured alloys using continuum damage mechanics. Proc. Inst. Mech. Eng, Part L:J. Mater.: Design Appl. 14644207211013434.

N'souglo, K.E., Rodríguez-Martínez, J.A., Vaz-Romero, A., Cazacu, O., 2019. The combined effect of plastic orthotropy and tension–compression asymmetry on the development of necking instabilities in flat tensile specimens subjected to dynamic loading. Int. J. Solids Struct. 159, 272–288.

Nygårds, M., 2009. Modelling the out-of-plane behaviour of paperboard. Nord. Pulp Paper Res. J. 24 (1), 72–76. http://dx.doi.org/10.3183/npprj-2009-24-01-p072-076.

Nygårds, M., Just, M., Tryding, J., 2009. Experimental and numerical studies of creasing of paperboard. Int. J. Solids Struct. 46 (11), 2493–2505. http://dx.doi.org/10.1016/j.ijsolstr.2009.02.014.

Ottosen, N.S., Ristinmaa, M., 2005. The Mechanics of Constitutive Modeling. Elsevier Science Ltd, http://dx.doi.org/10.1016/B978-0-08-044606-6.X5000-0.

Rice, J., 1976. Localization of plastic deformation. Theor. Appl. Mech. 207–220.

Rigdahl, M., Westerlind, B., Hollmark, H., 1984. Analysis of cellulose networks by the finite element method. J. Mater. Sci. (19), 3945–3952. http://dx.doi.org/10.1007/BF00980758.

Roberts, J.C., 1996. Cellulose fibre networks. In: The Chemistry of Paper. The Royal Society of Chemistry, pp. 52–68. http://dx.doi.org/10.1039/9781847552068-00052.

Robertsson, K., Borgqvist, E., Wallin, M., Ristinmaa, M., Tryding, J., Giampieri, A., Perego, U., 2018. Efficient and accurate simulation of the packaging forming process. Packag. Technol. Sci. 31, http://dx.doi.org/10.1002/pts.2383.

Rudnicki, J., Rice, J., 1975. Condition for the localization of deformation in pressure-sensitive dilatant materials. J. Mech. Phys. Solids 23, 371–394. http://dx.doi.org/10.1016/0022-5096(75)90001-0.

Ryou, H., Chung, K., Yu, W.-R., 2007. Constitutive modeling of woven composites considering asymmetric/anisotropic, rate dependent, and nonlinear behavior. Composites A 38 (12), 2500–2510.

Schemmann, M., Gajek, S., Böhlke, T., 2018a. Biaxial tensile tests and microstructure-based inverse parameter identification of inhomogeneous SMC composites. In: Advances in Mechanics of Materials and Structural Analysis. Springer, pp. 329–342.

Schemmann, M., Lang, J., Helfrich, A., Seelig, T., Böhlke, T., 2018b. Cruciform specimen design for biaxial tensile testing of SMC. J. Compos. Sci. 2 (1), 12.

Seidlhofer, T., Czibula, C., Teichert, C., Hirn, U., Ulz, M.H., 2021. A compressible plasticity model for pulp fibers under transverse load. Mech. Mater. 153, 103672.

Simo, J.C., Hughes, T.J., 2006. Computational Inelasticity, Vol. 7. Springer Science & Business Media.

Smits, A., Van Hemelrijck, D., Philippidis, T., Cardon, A., 2006. Design of a cruciform specimen for biaxial testing of fibre reinforced composite laminates. Compos. Sci. Technol. 66 (7), 964–975. http://dx.doi.org/10.1016/j.compscitech.2005.08.011.

Sowerby, R., Uko, D., Tomita, Y., 1979. A review of certain aspects of the Bauschinger effect in metals. Mater. Sci. Eng. 41 (1), 43–58.

Srinivasa, P., Kulachenko, A., 2015. Analysis of the compressive response of nano fibrillar cellulose foams. Mech. Mater. 80, 13–26. http://dx.doi.org/10.1016/j.mechmat.2014.09.006.

Stenberg, N., 2003. A model for the through-thickness elastic–plastic behaviour of paper. Int. J. Solids Struct. 40 (26), 7483–7498. http://dx.doi.org/10.1016/j.ijsolstr.2003.09.003.

Tjahjanto, D., Girlanda, O., Östlund, S., 2015. Anisotropic viscoelastic–viscoplastic continuum model for high-density cellulose-based materials. J. Mech. Phys. Solids 84, 1–20. http://dx.doi.org/10.1016/j.jmps.2015.07.002.

Tsai, S.W., Wu, E.M., 1971. A general theory of strength for anisotropic materials. J. Compos. Mater. 5 (1), 58–80.

Verma, P., Shofner, M., Griffin, A., 2014. Deconstructing the auxetic behavior of paper. Phys. Status Solidi (B) 251, http://dx.doi.org/10.1002/pssb.201384243.

VIC, 2021. Correlated Solutions – VIC-2D, URL https://www.correlatedsolutions.com/vic-2d/.

Wang, W., Liu, L., Ding, N., Zhang, R., Yu, J., 2021. Mechanical and thermal behavior analysis of wood–polypropylene composites. Text. Res. J. 91, 347–357. http://dx.doi.org/10.1177/0040517520944246.

Xia, Q.S., Boyce, M.C., Parks, D.M., 2002. A constitutive model for the anisotropic elastic–plastic deformation of paper and paperboard. Int. J. Solids Struct. 39 (15), 4053–4071. http://dx.doi.org/10.1016/S0020-7683(02)00238-X.

Zhao, K., Chen, L., Xiao, R., Ding, Z., Zhou, L., 2019. Design of a biaxial tensile testing device and cruciform specimens for large plastic deformation in the central zone. J. Mater. Sci. 54, http://dx.doi.org/10.1007/s10853-019-03358-2.